Journal of The Electrochemical Society, 2021 **168** 086505

FeOOH Modified H-TiO_2 Nanorods Array (NRA) for Stable and Improved Low-Bias Photoelectrochemical Water Splitting

Gabriele Panzeri,[1] Ruben Dell'Oro,[1] Alberto Panzeri,[1] Maurizio Sansotera,[1] Valeria Russo,[2] Claudia L. Bianchi,[3] and Luca Magagnin[1,z]

[1]*Department of Chemistry, Materials and Chemical Engineering Giulio Natta Politecnico di Milano, 20131 Milano, Italy*
[2]*Department di Energy and NEMAS—Center for NanoEngineered Materials and Surfaces Politecnico di Milano, 20133 Milano, Italy*
[3]*Department of Chemistry, Università degli Studi di Milano, 20133 Milano, Italy*

Iron oxyhydroxide (FeOOH) was implemented as a low-cost, stable, and earth-abundant catalyst on hydrogenated titania nanorods array (H-TiO_2/FeOOH), for photoelectrochemical water splitting applications. The hydrogenation treatment enhanced the maximum photocurrent density delivered by the titania-based photoanode (from 0.65 mA cm^{-2} to 1 mA cm^{-2} at +1.23 V vs RHE) while the exploitation of FeOOH resulted in a significant improvement in the photoelectrochemical activity at low bias. The optimized photoelectrode showed ~0.6 mA cm^{-2} at +0.4 V vs RHE, with a saturation current density of 1.05 mA cm^{-2}. Insights on the role of FeOOH were revealed by electrochemical impedance and photoluminescence measurements, suggesting a reduction of the charge transfer resistance at the electrolyte interface and a lower frequency of recombination events. The H-TiO_2/FeOOH photoelectrode showed a maximum applied bias photon-to-current efficiency (ABPE) of 0.68% with a 0.3 V bias, while for the bare TiO_2 nanorods array the maximum value of 0.4% was found at a bias of 0.4 V. A stable photocurrent was measured in 1 M NaOH solution through a 5 h test at 1.23 V vs RHE, under illumination (1 sun), suggesting the compatibility of FeOOH in highly alkaline solutions.
 [DOI: 10.1149/1945-7111/ac1b4b]

Manuscript submitted May 13, 2021; revised manuscript received June 23, 2021. Published August 16, 2021.

Supplementary material for this article is available online

Since the first demonstration of photoelectrochemical water splitting by Fujishima and Honda in 1972,[1] titania (TiO_2) has been extensively studied and it is considered one of the most promising photoanodes[2,3] because of its low cost and chemical/electrochemical stability in the entire pH window. Moreover, titania is also exploited for the decomposition of organic pollutants because of its high photocatalytic activity.[4–6] Despite these advantages, its large bandgap (E_b~3–3.2 eV) limits the portion of the solar spectrum absorbed, resulting in lower theoretical maximum photocurrent density values (j_{ph_max}~1.86 mA cm^{-2}) if compared to other photoanodes e.g. $BiVO_4$ (E_b~2.4 eV, j_{ph_max}~7.5 mA cm^{-2}), Fe_2O_3 (E_b~2.2 eV, j_{ph_max}~10.6 mA cm^{-2}).[7–9] To cope with these limitations, one-dimensional morphologies, such as nanotubes or nanorods, are typically exploited to increase light absorption and to improve the electrical pathway for the photogenerated charges.

Titania nanorods arrays (TiO_2 NRA) can be obtained through hydrothermal synthesis, resulting in the formation of (101) oriented rutile rods thanks to the small lattice mismatch with Fluorine doped Tin Oxide (FTO) substrate.[10] The rutile crystal phase is characterized by a bandgap (3.0 eV) smaller than the anatase one (3.2 eV),[11] harvesting also part of the radiation in the lower wavelength part of the visible spectrum ($\lambda \lesssim 413$ nm). Another strategy to increase the photogenerated charges consists of the doping of the TiO_2, achieved through the introduction of impurities atoms, such as transition metals and non-metals.[12] A chemically defected structure may result in the modification of the electrical properties of the material by introducing energy states between the conduction and valence bands. While the formation of deep impurity states in the middle of the bandgap acting as traps would increase the recombination rate, the introduction of shallow levels, lying close to the band edges, would result in a reduction of the actual bandgap of the material, capable to absorb photons with larger wavelengths. A well-known doping process is the hydrogenation treatment, which induces oxygen vacancies and surface hydrogenation, improving the absorption and the photocatalytic activity.[13,14] Wang et al. firstly demonstrated the effectiveness of annealing in a hydrogen-containing atmosphere of a TiO_2 nanorod array photoanode, showing a striking improvement in the photocurrent.[15] Moreover, the implementation of a catalytic material, aimed to enhance the charge transfer from the semiconductor surface to the electrolyte, is a consolidated strategy to improve the overall photoelectrochemical behavior.[16] However, only a few literature studies exploited this approach in the case of titania nanorods,[17–22] while in the cases of $BiVO_4$[23,24] and Fe_2O_3,[25,26] earth-abundant NiOOH and FeOOH catalysts[27] have been extensively investigated.

In this study, we photo-electrodeposited earth-abundant and low-cost FeOOH catalyst onto a hydrogenated TiO_2 nanorods array. The combination of hydrogenation treatment with an oxygen evolution reaction (OER) catalyst enhanced the photoelectrochemical behavior showing a significant photocurrent increase also under a low bias, which is particularly important in a hypothetical tandem configuration.[28–30] In this case, the bias-free working condition is determined at the intersection of the j–V characteristics of photoanode and photocathode. For this reason, the TiO_2 cathodic onset potential, allowed by the low position of the valence band, combined with a significative photocurrent output at low bias is suitable to determine better overall device performances. Eventually, the reliability of the FeOOH catalyst is demonstrated by testing the H-TiO_2/FeOOH photoelectrode in a strongly alkaline solution, suitable for the electrolysis process.

Experimental

TiO_2 hydrothermal synthesis.—Fluorine-doped Tin Oxide (FTO) coated glass (Aldrich, 300 mm × 300 mm × 2.2 mm, surface resistivity 7 Ω sq^{-1}) was used as a substrate. The FTO was sonicated for 20 min in a 1:1:1 vol. mixture of deionized water, acetone (Sigma-Aldrich, purity 99%), and propanol (Sigma-Aldrich, purity 99.5%). A portion of the FTO substrate was covered with PTFE tape to guarantee good electrical contact for the photoelectrode. The cleaned substrate was placed in a 100 ml Teflon-lined reactor, inclined against the wall with the conductive face facing up, filled with a solution composed of 20 ml of deionized water, 20 ml of hydrochloric acid (Sigma-Aldrich, purity 37.5%), and 0.67 ml of titanium n-butoxide (Aldrich, purity 97%), previously left under stirring for 15 min. The autoclave was placed in a laboratory oven and maintained at 150 °C for 5 h, setting a heating ramp of 5 °C min^{-1}. The sample was removed from the autoclave and washed

[z]E-mail: luca.magagnin@polimi.it

with a copious amount of water to remove all the possible remains of the synthesis solution from the nanorod array. Finally, the nanorods were annealed on a plate at 500 °C for 30 min in an air atmosphere.

TiO_2 hydrogenation.—The hydrogenation of TiO_2 nanorods was performed in a tubular furnace using a 3 cm diameter quartz tube. An 80% v/v argon and 20% v/v hydrogen atmosphere was obtained by fluxing 4 Nl h^{-1} of Ar and 1 Nl h^{-1} of H_2 in the vial, which was inserted directly in the furnace previously heated at 350 °C. After 30 min the vial was removed from the oven and let cool, after switching off the hydrogen flux.

FeOOH photo-electrodeposition.—After hydrogenation, the iron oxyhydroxide (FeOOH) catalyst was deposited by photoassisted electrodeposition, using an aqueous solution containing 5–100 mM $FeSO_4{\cdot}7\ H_2O$ (Sigma-Aldrich, purity 99%). A freshly prepared solution was employed for every batch tested due to its limited time stability, precipitation is likely to occur over time. The setup featured a three-electrode configuration with a TiO_2 nanorods array as a working electrode (WE), a platinum-coated titanium net as a counter electrode (CE), and an Ag/AgCl (3 M KCl) reference electrode (RE). The photo-electrodeposition was carried out at +0.25 V vs Ag/AgCl for 5 min with a potentiostat (AMEL 2559), under constant 100 mW cm^{-2} (AM 1.5 G) illumination using an ABET 83 SunLite solar simulator 11002, equipped with a 100 W Xenon arc lamp.

Materials characterization.—XRD measurements were carried out with a Malvern Panalytical EMPYREAN diffractometer. The measurements were done in thin-film mode with $K\alpha 1_{Cu} = 1.54058$ Å. SEM micrographs were obtained using a ZEISS EVO 50 EP, equipped with an OXFORD INCA ENERGY 200 EDS unit. XPS measurements were performed with an M-Probe—Surface Science Instrument employing an un-monochromatized Al Kα source (photon energy = 1486.6 eV) at normal emission and room temperature. For high-resolution analysis, 1 s level hydrocarbon-contaminant carbon was taken as the internal reference at 284.6 eV. Fittings were performed using pure Gaussian peaks, Shirley's baseline, and without any constraints. The photoelectrons were collected with a pass energy of 20 eV for high-resolution spectra and 40 eV for wide spectra. The overall FWHM resolution of the combined photon source and the spectrometer is below 1 eV. Micro-Raman and photoluminescence (PL) measurements were performed with a Renishaw In Via spectrometer equipped with an Ar^+ laser, $\lambda = 514.5$ nm, keeping the power on the sample below 1 mW. A quantitative evaluation of the amount of catalyst deposited was performed with inductively coupled plasma–optical emission spectrometry (ICP-OES) Perkin Elmer Optima 8300. The photoelectrochemical behavior was assessed through linear scan voltammetries (LSV) with a three-electrode cell including photoelectrode (WE), platinum net (CE), and Ag/AgCl (3 M KCl) (RE) immersed in a 1 M NaOH solution (pH = 13.6). The measurements were acquired with AMEL 2559 potentiostat setting 10 mV s^{-1} scan rate, under constant AM 1.5 G light radiation using an ABET 83 SunLite solar simulator 11002.

Results and Discussion

TiO_2 nanorods array.—The synthesis of a dense array of TiO_2 nanorods through a hydrothermal process was optimized based on the previous literature works.[10,15] A homogenous coverage over a large area sample (3 × 4 cm^2) was obtained at a heating ramp of 5 °C min^{-1} and a reaction temperature of 150 °C (Fig. 1a). SEM

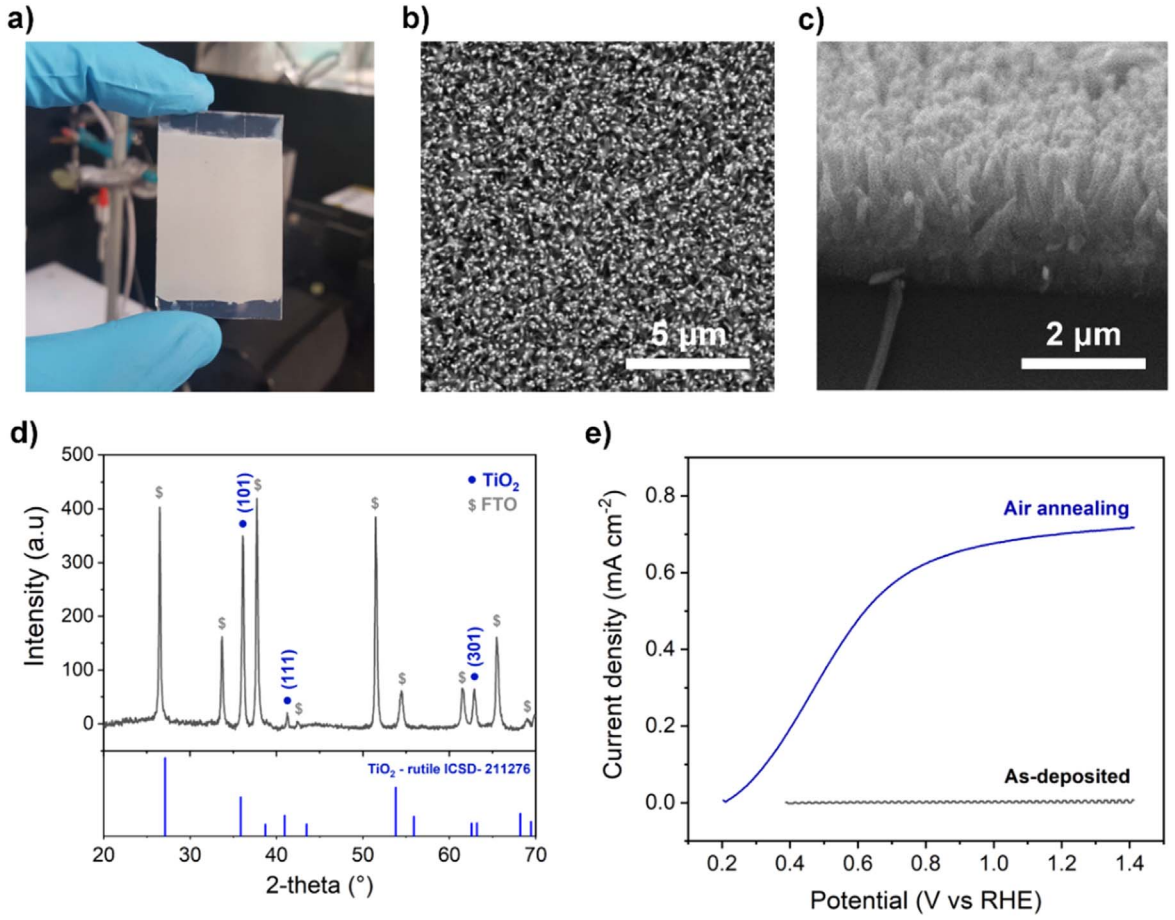

Figure 1. TiO_2 nanorods array (a) Real pic of the sample (b-c) SEM micrographs. (d) XRD pattern of the TiO_2 after air annealing and reference pattern of the rutile phase. (e) Anodic linear sweep voltammetry of TiO_2 nanorods photoelectrode, before and after air annealing, under AM 1.5 G illumination [100 mW cm^{-2}] in 1 M NaOH solution.

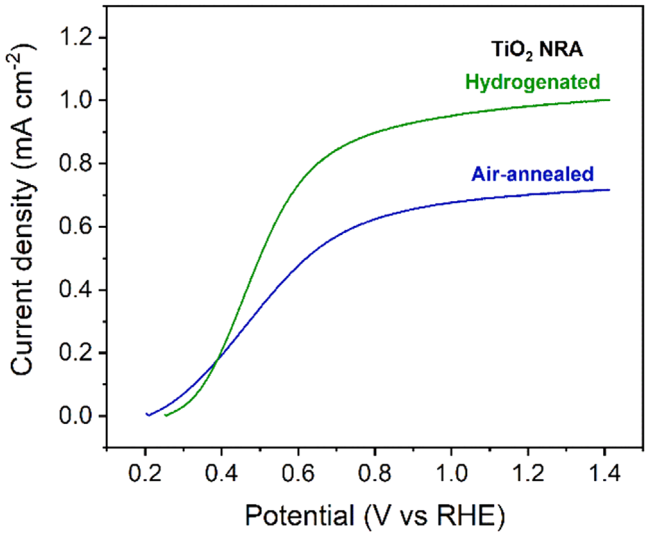

Figure 2. Anodic linear sweep voltammetry of TiO_2 nanorods array (NRA) photoelectrode, air annealed and hydrogenated, under AM 1.5 G illumination [100 mW cm^{-2}] in 1 M NaOH solution.

micrographs showed the characteristic tetragonal shape of TiO_2 nanorods, having diameters in the range of 100–200 nm and a length of about 1–1.5 μm (Figs. 1b,1c). The annealing conditions were selected according to literature data and the optimal parameters were defined based on the photoelectrochemical response (Figs. S1–S2 available online at stacks.iop.org/JES/168/086505/mmedia). Air annealing at 500 °C greatly improved the photoelectrochemical behavior with respect to lower temperature treatments: a relatively short annealing time (30 min) was already effective in improving the semiconductor properties of the nanorods (Figs. S1–2). The annealing step was fundamental to adjust the stoichiometry of the material and to improve the crystallinity of the rutile phase, whose diffraction peaks (2θ = 36.1°, 41.3°, 62.9°) resulted to be well defined and sharp (Fig. 1d). The relative intensities of the peaks indicated the preferential orientation of the nanorods along (101), in agreement with the SEM micrographs (Figs. 1b–1d). Therefore, the open-circuit potential under illumination was shifted towards more negative potential values (0.2 V vs RHE) and the saturation current density reached ~0.65 mA cm^{-2} at 1.23 V vs RHE.

Effect of hydrogenation.—The hydrogenation treatment was introduced to improve the photoelectrochemical activity of the TiO_2 nanorods. The annealing in a reductive environment is expected to increase the density of oxygen vacancies,[13,14] which have a critical role in determining the surface and electrical properties, such as light absorption, electrical conductivity, and charge transport. Different annealing temperatures were investigated (250 °C–450 °C) while mantaining thereducing atmosphere at 20% v/v H_2 and 80% v/v Ar. The intermediate temperature (350 °C) introduced an enhancement of the photoelectrical behavior of the TiO_2 nanorods, increasing the saturation photocurrent density to 1 mA cm^{-2} and improving the fill factor of the curve (Fig. 2). Hydrogenation treatment to 250 °C was insufficient to produce a significant change, whereas the performances dropped after the hydrogenation at 450 °C (Fig. S3). In the latter case, the reduction in photocurrent density may be accounted to an excessive introduction of oxygen vacancies, inducing a significant recombination phenomenon at defect states acting as trap sites, or to an initial reduction of F:SnO_2 layer to metallic Sn in the FTO substrate, increasing its resistivity.[15,31] Raman and PL analysis was performed to investigate the modification induced by the annealing treatments. The Raman spectra of TiO_2 nanorods after hydrothermal synthesis, air annealing, and hydrogenation are reported in Fig. 3a. They all show the peculiar features of rutile TiO_2, located at about 235 cm^{-1}, 445 cm^{-1}, and

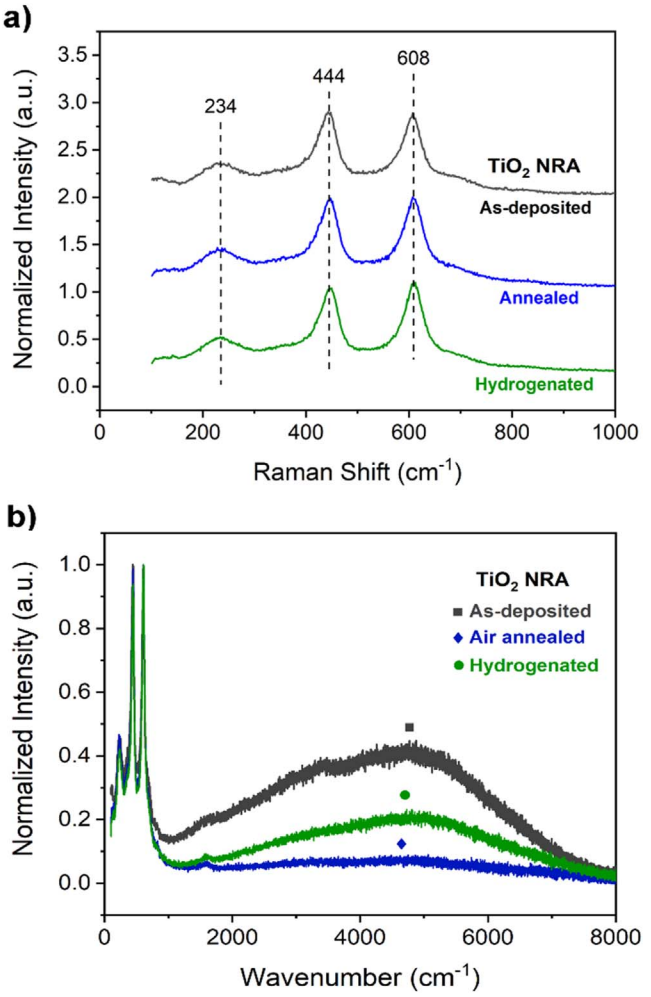

Figure 3. As-deposited, air annealed, and hydrogenated TiO_2 nanorods array (NRA) (a) Raman spectrum. (b) photoluminescence spectrum.

611 cm^{-1},[32] confirming the XRD results previously described. The relative intensity of the two major peaks slightly changes after treatments, while their position and width remained unchanged, suggesting minor modifications in the rutile structure. The large peaks' characteristics of rutile TiO_2 substantially change only in presence of a high defectivity or strong confinement effect, in contrast to the anatase phase whose very sharp Raman peaks shift or change in shape due to minor modification of the structure.[32] On the other hand, PL measurements (Fig. 3b) revealed differences in the material before and after the treatments: the as-synthesized nanorods showed a broad PL band in the red region of the visible (at about 1.8 eV), suggesting the presence of states within the energy gap due to defects and oxygen vacancies.[33] As expected, the PL signal was drastically reduced by the annealing treatment in air, which improved the sample crystallinity through rearrangement of the atoms and filling of the oxygen vacancies. Conversely, during hydrogenation, the formation of acceptor-type defects and oxygen reduction is expected, resulting in states within the energy gap and a consequent intensification of the PL band.

Besides, XPS analysis of the air annealed and hydrogenated samples was performed at low binding energy, to obtain information on the position of the valence band. The presence of a band tail at about 0.3 eV agreed with the formation of acceptor-type defects within the bandgap, shifting the valence band edge from 2.04 to 1.37 eV (Fig. 4). According to IPCE[34–36] and UV-vis[37] data on hydrogenated TiO_2 NRAs reported in the literature, the formation of electronic defect states within the bandgap results in a significant enhancement in the visible light absorption for $\lambda < 425$ nm. This

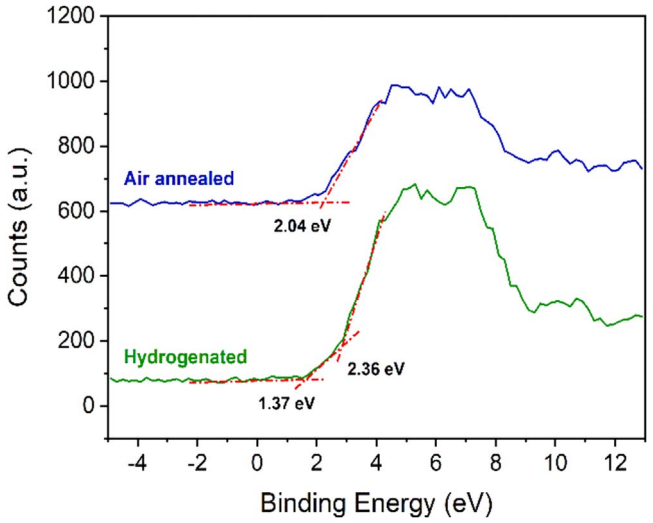

Figure 4. XPS valence band spectra of air annealed and hydrogenated TiO_2 nanorods array (NRA).

result agrees with the higher saturation photocurrent density observed in the photoelectrochemical characterization (Fig. 2).

FeOOH catalyst implementation.—The iron oxyhydroxide (FeOOH) catalyst was deposited onto the H-TiO_2 nanorods through photo-electrodeposition at 0.25 V vs Ag/AgCl for 5 min using an iron sulfate solution. Both XRD and SEM analyses were unable to show any change in microstructure and morphology after the catalyst deposition, due to the small amount of deposited material. To determine the catalyst composition and elemental oxidation state, XPS was carried out (Fig. 5a).[38] High-resolution XPS analysis in the region of Ti *2p* peaks revealed that after catalyst deposition H-TiO_2 nanorods remained unaltered showing the typical double signal system of pure titanium dioxide with Ti $2p_{3/2}$ and Ti $2p_{1/2}$ at 458.5 and 464.2 eV (Fig. 5b), respectively.[17] The region of O *1 s* signals was also observed by high-resolution XPS analysis and H-TiO_2 nanorods showed a peak that can be fitted in two contributions (Fig. 5c): one at 529.9 eV ascribable to oxygen as oxide and another at 531.6 eV due to hydroxyl groups.[39] Due to the deposition of the FeOOH catalyst, the characteristic region of Fe *2p* (Fig. 5d) was also investigated and the peaks of Fe $2p_{3/2}$ and Fe $2p_{1/2}$ at around 711 and 724 eV were observed.[40,41] These signals are in the typical range of Fe^{3+} of iron oxyhydroxide and the broad shape of Fe $2p_{3/2}$ peak corresponded to the literature data on FeOOH.[42–44] FeOOH peaks are usually assigned as a single $2p_{3/2}$ and $2p_{1/2}$ system, even if two contributions in each signal can be distinguished: at 710.6 and 712.5 eV for Fe $2p_{3/2}$, and 723.9 and 725.7 eV for Fe $2p_{1/2}$. The former can be ascribed to an electronic shift due to oxidic O; the latter to interactions with hydroxylic O.

The best results in terms of photoelectrochemical performances were obtained using a dilute solution (5 mM), resulting in a deposition charge of ~25 mC cm^{-2} (measured as total charge passing through the system). Catalyst loading was measured using ICP-OES on a 2 × 2 cm^2 sample area, ~1.64 $\mu g\ cm^{-2}$ of FeOOH was measured. The catalyst improved significantly the photocurrent delivered at low overpotentials and shifted the onset potential, arbitrarily evaluated at 0.1 mA cm^{-2}, from 0.35 V vs RHE to

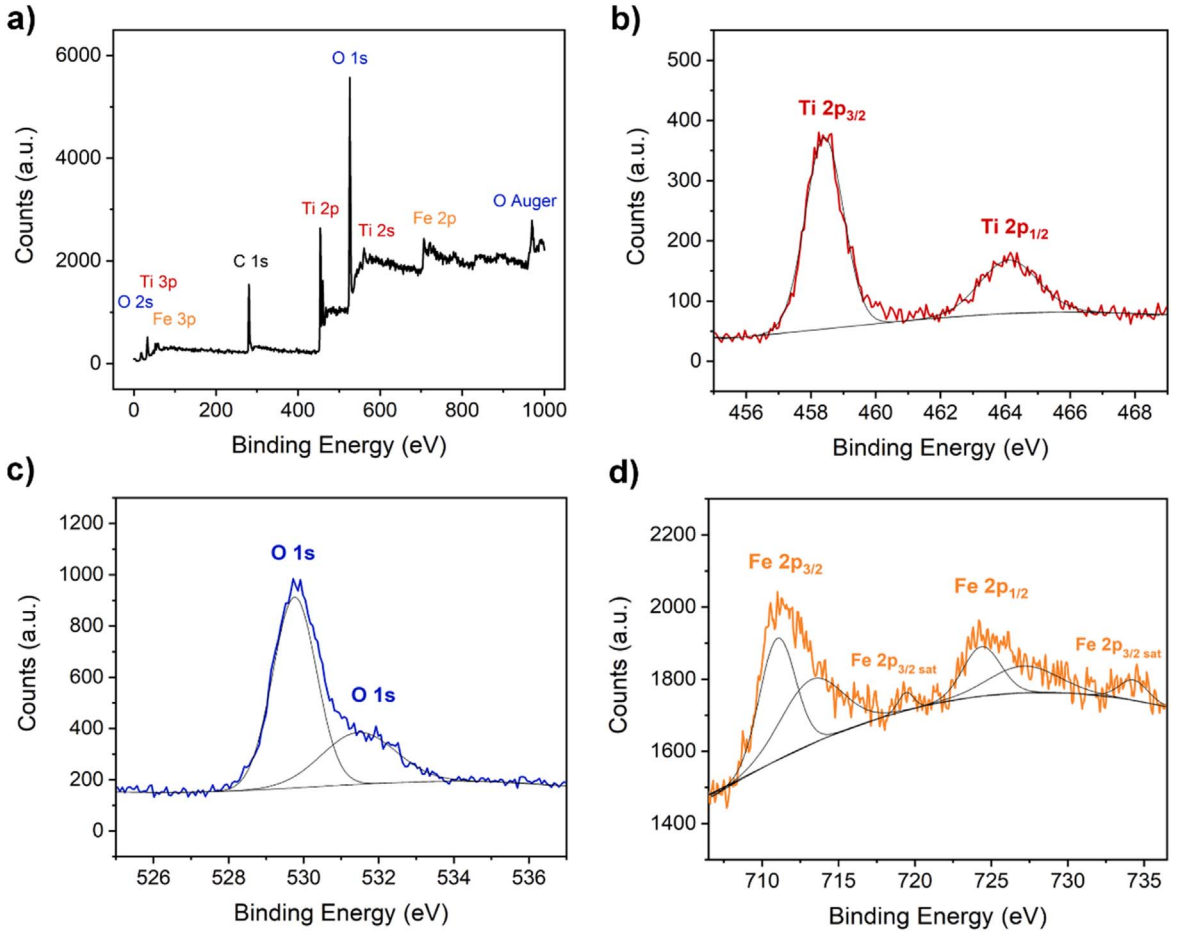

Figure 5. XPS spectra of hydrogenated titania nanorods array (NRA) with iron oxyhydroxide catalyst (H-TiO_2/FeOOH). (a) Survey. (b) Ti 2p. (c) O 1 s. (d) Fe 2p.

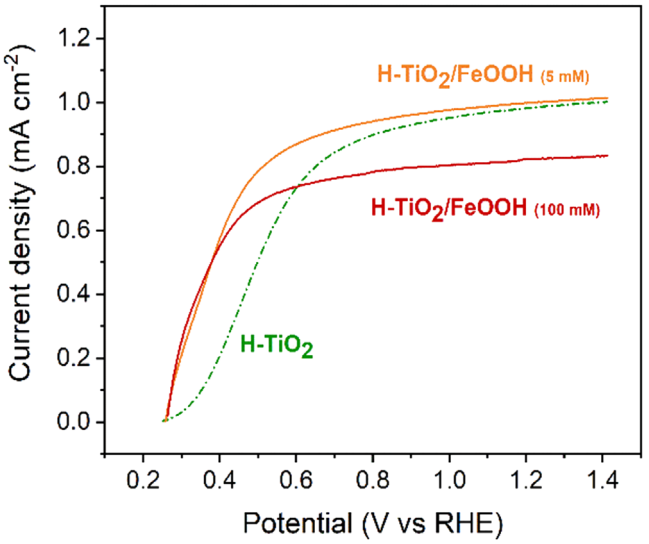

Figure 6. Anodic linear sweep voltammetry of hydrogenated titania nanorods array (H-TiO_2), with and without FeOOH catalyst, under AM 1.5 G illumination [100 mW cm^{-2}] in 1 M NaOH solution. 5 mM and 100 mM refer to the Fe^{3+} concentration in the photo-electrodeposition solution.

0.28 V vs RHE (Fig. 6). On the other hand, at higher catalyst loading the maximum current delivered was reduced to 0.8 mA cm^{-2} while the same immersion potential under illumination and curve feature at low overpotential was maintained (Fig. 6). A similar trend was found in the case of cobalt phosphate (Co-Pi) catalyst photo-electrodeposited onto a titania nanorod array.[17] At high catalyst loading, the onset potential remained unchanged while the saturation current was reduced.

To better visualize the effect of the hydrogenation treatment and the FeOOH catalyst in the low-bias region, the photoelectrodes were tested in a two-electrode cell using a platinum-coated titanium mesh as the counter electrode (Fig. 7). The cell voltage was progressively increased starting from the open circuit value i.e. bias-free condition. The applied bias photon-to-current efficiency (ABPE), for the two-electrodes photoelectrochemical cell, can be defined as follows:[45]

$$ABPE\ (\%) = \frac{j_{ph}\,(E^0 - V)}{P_{light}} 100$$

Where j_{ph} [mA cm^{-2}] is the photocurrent density measured at the cell applied bias V [V], E^0 is the thermodynamic voltage for the water electrolysis process ($E^0 = 1.23$ V) and P_{light} is the radiation power density (100 mW cm^{-2}). In this configuration, the anodic/cathodic overpotentials and the ohmic drops are considered, which is a requirement for the calculation of the device's photoconversion efficiency. It is important to notice that the equation cannot be applied in the case of a three-electrode configuration which serves the only purpose of investigating the photoelectrochemical behavior of a half-cell rather than a device.[45] The photocurrent density values measured agreed with the previous photoelectrochemical characterization although a lower fill factor of the curve is shown as expected (Fig. 7a) since the cathodic overpotentials and ohmic drops are also included. The hydrogenation treatment and subsequent FeOOH deposition progressively increased the maximum ABPE value recorded from 0.4% to 0.68%, which is observed at an applied bias of only about 0.3 V in the case of the H-TiO_2/FeOOH photoelectrode (Fig. 7b).

The presence of the catalysts on the surface reduced the recombination events of the photogenerated charges, as shown by the quenching of the photoluminescence observed (Fig. 8a). This reduction could not be explained by a microstructure modification of

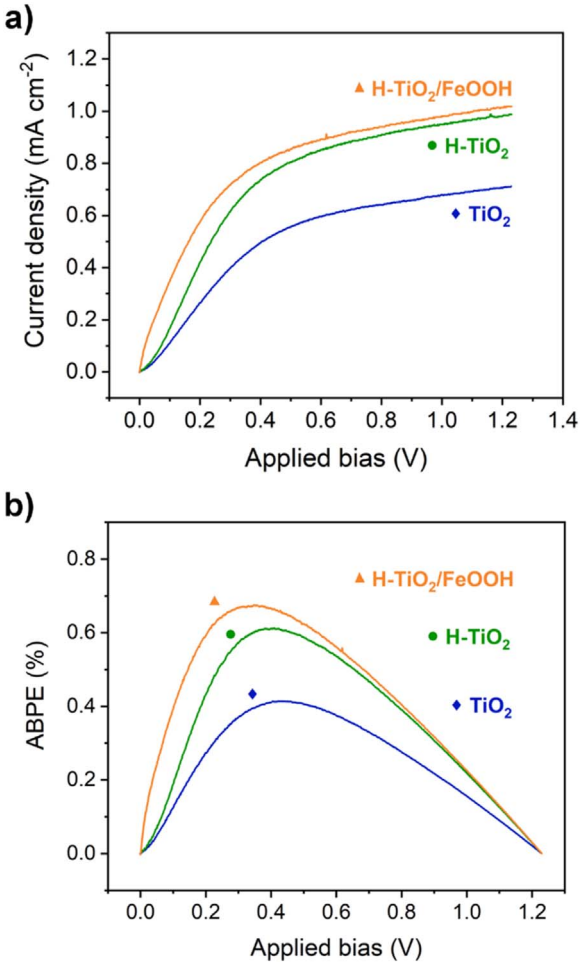

Figure 7. (a) Linear sweep voltammetry of a two-electrode cell comprising the titania nanorods (NRA) based photoelectrode, as the working electrode, and a platinum-coated titanium mesh as the counter electrode. (b) Applied bias photoconversion efficiency (ABPE) of TiO_2, H-TiO_2, and H-TiO_2/FeOOH photoelectrodes under AM 1.5 G illumination [100 mW cm^{-2}] in 1 M NaOH solution.

the hydrogenated nanorods since the deposited catalyst is not expected to remove the trap sites introduced by the hydrogenation acting as recombination sites. This behavior may be correlated to the position of the electronic bands of the catalyst, slightly above the valence band of the hydrogenated TiO_2.[46,47] So, the photogenerated holes in the hydrogenated TiO_2 were favored to be transferred in the catalyst layers. The charge transfer from the semiconductor surface to the electrolytic solution was studied through electrochemical impedance spectroscopy (EIS) to highlight the role of the FeOOH (Fig. 8b). The measurements were carried out under illumination, at the open circuit potential.[18,48] The Nyquist plot showed a significant reduction in the charge transfer resistance i.e. semicircle diameter, for the modified H-TiO_2 nanorods with respect to the bare one. This result demonstrates that the FeOOH improved the charge transfer, resulting in a higher photocurrent density at a low bias (Fig. 8b).

The catalyst stability was evaluated through a 5-hour long test in which the photoelectrode surface potential was kept at + 1.23 V vs RHE, under constant illumination (Fig. 9). Working under saturation conditions maximized the working current density, assessing the photostability in the worst scenario. The photocurrent density stabilized at 1.05 mA cm^{-2} and remained constant for all the duration of the test, indicating that no secondary oxidation processes (i.e. degradation of the catalytic layer) occurred. The results agreed with the literature data, reporting the electrochemical stability of FeOOH catalyst in highly alkaline solutions, under anodic polarization.[49,50] Besides, it is

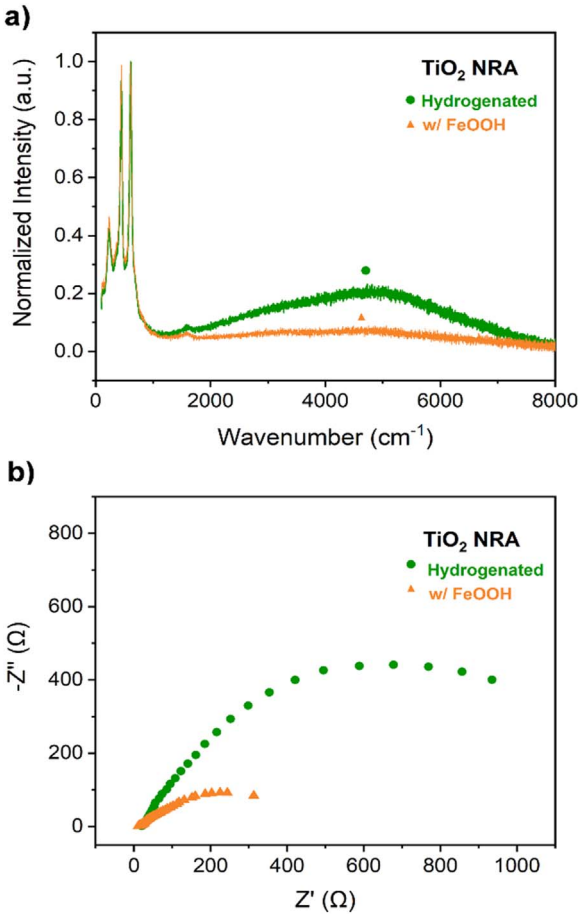

Figure 8. Effect of FeOOH catalyst on hydrogenated titania nanorods array (NRA). (a) Photoluminescence spectrum. (b) Electrochemical impedance spectroscopy graph as Nyquist plots. The test was carried out at the open circuit potential under AM 1.5 G illumination [100 mW cm^{-2}] in 1 M NaOH solution.

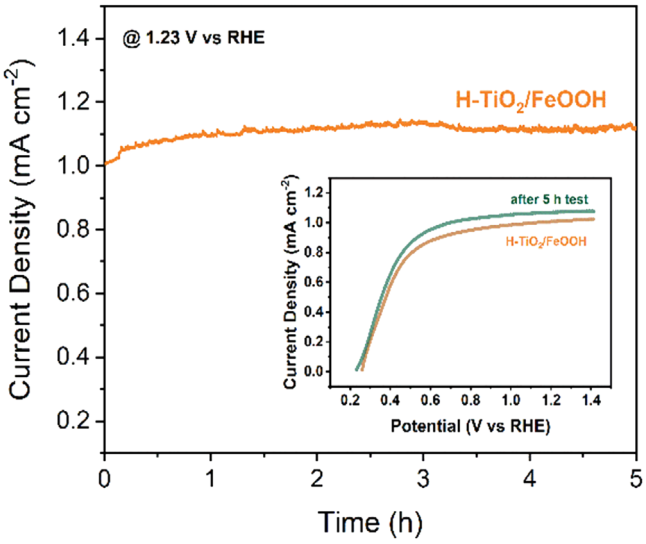

Figure 9. Stability test of the FeOOH-modified nanorods array photoelectrode (H-TiO_2/FeOOH) in 1 M NaOH solution at 1.23 V vs RHE, under AM 1.5 G illumination [100 mW cm^{-2}]. Inset: anodic linear sweep voltammetry of the photoelectrode before and after the test.

important to notice that any variation of the photocurrent density delivered by the photoanode is not affecting the Faradaic efficiency of the hydrogen evolution reaction, occurring at the platinum counter surface. To confirm the integrity of the FeOOH catalyst, the photoelectrochemical behavior was analyzed right after the stability test. The LSV curve showed the same characteristic at low-bias, before reaching the saturation current density value, indicating the catalytic activity remained unchanged (Fig. 9—inset).

Conclusions

In summary, we successfully implemented FeOOH onto the hydrogenated TiO_2 nanorods array. The catalyst was deposited by a facile photo-electrodeposition method, based on earth-abundant elements and compatible with large area fabrication. The best performances were found carrying out the photoassisted deposition in a more diluted solution (5 mM), which resulted in an improved charge transfer and lower recombination. The H-TiO_2/FeOOH photoelectrode showed ~0.6 mA cm^{-2} at 0.4 V vs RHE, 1.4 times higher than the catalyst-free photoelectrodes, with a saturation current density of ~1.05 mA cm^{-2} at 1.23 V vs RHE. The improved photoelectrochemical behavior was maintained also after a 5 h test under constant illumination (1 sun) at 1.23 V vs RHE, in 1 M NaOH solution.

ORCID

Gabriele Panzeri https://orcid.org/0000-0003-3460-7786
Ruben Dell'Oro https://orcid.org/0000-0003-1719-4860
Maurizio Sansotera https://orcid.org/0000-0001-5388-651X
Valeria Russo https://orcid.org/0000-0001-9543-0422
Claudia L. Bianchi https://orcid.org/0000-0002-9702-6949
Luca Magagnin https://orcid.org/0000-0001-5553-6441

References

1. A. Fujishima and K. Honda, "Electrochemical photolysis of water at a semiconductor electrode." *Nature*, **238**, 37 (1972).
2. K. Shankar, J. I. Basham, N. K. Allam, O. K. Varghese, G. K. Mor, X. Feng, M. Paulose, J. A. Seabold, K. S. Choi, and C. A. Grimes, "Recent advances In the use of TiO2 nanotube and nanowire arrays for oxidative photoelectrochemistry." *J. Phys. Chem. C*, **113**, 6327 (2009).
3. Y. Xie, "Photoelectrochemical application of nanotubular titania photoanode." *Electrochim. Acta*, **51**, 3399 (2006).
4. G. Liu, L. Wang, H. G. Yang, H. M. Cheng, and G. Q. Lu, "Titania-based photocatalysts - Crystal growth, doping and heterostructuring." *J. Mater. Chem.*, **20**, 831 (2010).
5. A. Y. C. Tong, R. Braund, D. S. Warren, and B. M. Peake, "TiO2-assisted photodegradation of pharmaceuticals - A review." *Cent. Eur. J. Chem.*, **10**, 989 (2012).
6. U. I. Gaya and A. H. Abdullah, "Heterogeneous photocatalytic degradation of organic contaminants over titanium dioxide: A review of fundamentals, progress and problems." *J. Photochem. Photobiol. C Photochem. Rev.*, **9**, 1 (2008).
7. D. Kang, T. W. Kim, S. R. Kubota, A. C. Cardiel, H. G. Cha, and K. S. Choi, "Electrochemical synthesis of photoelectrodes and catalysts for use in solar water splitting." *Chem. Rev.*, **115**, 12839 (2015).
8. J. Su and L. Vayssieres, "A place in the sun for artificial photosynthesis?" *ACS Energy Lett.*, **1**, 121 (2016).
9. C. X. Kronawitter, L. Vayssieres, S. Shen, L. Guo, D. A. Wheeler, J. Z. Zhang, B. R. Antoun, and S. S. Mao, "A perspective on solar-driven water splitting with all-oxide hetero-nanostructures." *Energy Environ. Sci.*, **4**, 3889 (2011).
10. B. Liu and E. S. Aydil, "Growth of oriented single-crystalline rutile TiO2 nanorods on transparent conducting substrates for dye-sensitized solar cells." *J. Am. Chem. Soc.*, **131**, 3985 (2009).
11. S. Tanemura, L. Miao, P. Jin, K. Kaneko, A. Terai, and N. Nabatova-Gabain, "Optical properties of polycrystalline and epitaxial anatase and rutile TiO2 thin films by rf magnetron sputtering." *Appl. Surf. Sci., Elsevier*, **212–213**, 654 (2003).
12. Q. Meng, T. Wang, E. Liu, X. Ma, Q. Ge, and J. Gong, "Understanding electronic and optical properties of anatase TiO2 photocatalysts co-doped with nitrogen and transition metals." *Phys. Chem. Chem. Phys.*, **15**, 9549 (2013).
13. T. Leshuk, R. Parviz, P. Everett, H. Krishnakumar, R. A. Varin, and F. Gu, "Photocatalytic activity of hydrogenated TiO2." *ACS Appl. Mater. Interfaces*, **5**, 1892 (2013).
14. X. Yu, B. Kim, and Y. K. Kim, "Highly enhanced photoactivity of anatase TiO2 nanocrystals by controlled hydrogenation-induced surface defects." *ACS Catal.*, **3**, 2479 (2013).
15. G. Wang, H. Wang, Y. Ling, Y. Tang, X. Yang, R. C. Fitzmorris, C. Wang, J. Z. Zhang, and Y. Li, "Hydrogen-treated TiO2 nanowire arrays for photoelectrochemical water splitting." *Nano Lett.*, **11**, 3026 (2011).
16. I. Roger, M. A. Shipman, and M. D. Symes, "Earth-abundant catalysts for electrochemical and photoelectrochemical water splitting." *Nat. Rev. Chem.*, **1**, 1 (2017).
17. G. Ai, R. Mo, H. Li, and J. Zhong, "Cobalt phosphate modified TiO2 nanowire arrays as co-catalysts for solar water splitting." *Nanoscale.*, **7**, 6722 (2015).

18. Y. Pi, Z. Li, D. Xu, J. Liu, Y. Li, F. Zhang, G. Zhang, W. Peng, and X. Fan, "1T-phase MoS2 nanosheets on TiO2 nanorod arrays: 3D photoanode with extraordinary catalytic performance." *ACS Sustain. Chem. Eng.*, **5**, 5175 (2017).
19. W. M. A. El Rouby, M. Antuch, S. M. You, P. Beaunier, and P. Millet, "Novel nano-architectured water splitting photoanodes based on TiO2-nanorod mats surface sensitized by ZIF-67 coatings." *Int. J. Hydrogen Energy*, **44**, 30949 (2019).
20. H. Lin and L. Zhao, "Novel g-C3N4/TiO2 nanorods with enhanced photocatalytic activity for water treatment and H2 production." *J. Mater. Sci., Mater. Electron.*, **30**, 18191 (2019).
21. D. E. Schipper et al., "A TiO2/FeMnP core/shell nanorod array photoanode for efficient photoelectrochemical oxygen evolution." *ACS Nano.*, **11**, 4051 (2017).
22. P. Yilmaz, A. M. Lacerda, I. Larrosa, and S. Dunn, "Photoelectrocatalysis of rhodamine B and solar hydrogen production by TiO2 and Pd/TiO2 catalyst systems." *Electrochim. Acta*, **231**, 641 (2017).
23. J. A. Seabold and K. S. Choi, "Efficient and stable photo-oxidation of water by a bismuth vanadate photoanode coupled with an iron oxyhydroxide oxygen evolution catalyst." *J. Am. Chem. Soc.*, **134**, 2186 (2012).
24. T. W. Kim and K. S. Choi, "Nanoporous BiVO4 photoanodes with dual-layer oxygen evolution catalysts for solar water splitting." *Science (80).*, **343**, 990 (2014).
25. J. Xiao, L. Fan, Z. Huang, J. Zhong, F. Zhao, K. Xu, S. F. Zhou, and G. Zhan, "Functional principle of the synergistic effect of co-loaded Co-Pi and FeOOH on Fe2O3 photoanodes for photoelectrochemical water oxidation." *Chinese J. Catal.*, **41**, 1761 (2020).
26. C. Feng, S. Fu, W. Wang, Y. Zhang, and Y. Bi, "High-crystalline and high-aspect-ratio hematite nanotube photoanode for efficient solar water splitting." *Appl. Catal. B Environ.*, **257**, 117900 (2019).
27. R. Subbaraman, D. Tripkovic, K. C. Chang, D. Strmcnik, A. P. Paulikas, P. Hirunsit, M. Chan, J. Greeley, V. Stamenkovic, and N. M. Markovic, "Trends in activity for the water electrolyser reactions on 3d M(Ni,Co,Fe,Mn) hydr(oxy) oxide catalysts." *Nat. Mater.*, **11**, 550 (2012).
28. M. S. Prévot and K. Sivula, "Photoelectrochemical tandem cells for solar water splitting." *J. Phys. Chem. C*, **117**, 17879 (2013).
29. H. Zhang, H. Wang, and J. Xuan, "Rational design of photoelectrochemical cells towards bias-free water splitting: Thermodynamic and kinetic insights." *J. Power Sources*, **462**, 228113 (2020).
30. Y. Chen, X. Feng, Y. Liu, X. Guan, C. Burda, and L. Guo, "Metal oxide-based tandem cells for self-biased photoelectrochemical water splitting." *ACS Energy Lett.*, **5**, 844 (2020).
31. C. Ros, C. Fàbrega, D. Monllor-Satoca, M. D. Hernández-Alonso, G. Penelas-Pérez, J. R. Morante, and T. Andreu, "Hydrogenation and structuration of TiO2 nanorod photoanodes: doping level and the effect of illumination in trap-states filling." *J. Phys. Chem. C*, **122**, 3295 (2018).
32. A. Li Bassi et al., "Raman spectroscopy characterization of titania nanoparticles produced by flame pyrolysis: The influence of size and stoichiometry." *J. Appl. Phys.*, **98**, 074305 (2005).
33. L. Mascaretti, V. Russo, G. Zoppellaro, A. Lucotti, C. S. Casari, Š. Kment, A. Naldoni, and A. Li Bassi, "Excitation wavelength- and medium-dependent photoluminescence of reduced nanostructured TiO2 films." *J. Phys. Chem. C*, **123**, 11292 (2019).
34. S. Hoang, S. P. Berglund, N. T. Hahn, A. J. Bard, and C. B. Mullins, "Enhancing visible light photo-oxidation of water with TiO2 nanowire arrays via cotreatment with H2 and NH3: Synergistic effects between Ti 3 + and N." *J. Am. Chem. Soc.*, **134**, 3659 (2012).
35. H. Wang, G. Wang, Y. Ling, M. Lepert, C. Wang, J. Z. Zhang, and Y. Li, "Photoelectrochemical study of oxygen deficient TiO2 nanowire arrays with CdS quantum dot sensitization." *Nanoscale.*, **4**, 1463 (2012).
36. X. Wang et al., "Enhanced photoelectrochemical behavior of H-TiO2 nanorods hydrogenated by controlled and local rapid thermal annealing." *Nanoscale Res. Lett.*, **12**, 336 (2017).
37. S. Zhang, S. Zhang, B. Peng, H. Wang, H. Yu, H. Wang, and F. Peng, "High performance hydrogenated TiO2 nanorod arrays as a photoelectrochemical sensor for organic compounds under visible light." *Electrochem. Commun.*, **40**, 24 (2014).
38. J. Lefebvre, F. Galli, C. L. Bianchi, G. S. Patience, and D. C. Boffito, "Experimental methods in chemical engineering: X-ray photoelectron spectroscopy-XPS." *Can. J. Chem. Eng.*, **97**, 2588 (2019).
39. S. Gatto, M. Sansotera, F. Persico, M. Gola, C. Pirola, W. Panzeri, W. Navarrini, and C. L. Bianchi, "Surface fluorination on TiO2 catalyst induced by photodegradation of perfluorooctanoic acid." *Catal. Today*, **241**, 8 (2015).
40. A. M. Beccaria, G. Poggi, and G. Castello, "Influence of passive film composition and sea water pressure on resistance to localised corrosion of some stainless steels in sea water." *Br. Corros. J.*, **30**, 283 (1995).
41. T. L. Barr, "An ESCA study of the termination of the passivation of elemental metals." *J. Phys. Chem.*, **82**, 1801 (1978).
42. D. Brion, "Etude par spectroscopie de photoelectrons de la degradation superficielle de FeS2, CuFeS2, ZnS et PbS a l'air et dans l'eau." *Appl. Surf. Sci.*, **5**, 133 (1980).
43. B. Zhang, X. Huang, Y. Zhang, G. Lu, L. Chou, and Y. Bi, "Unveiling the activity and stability origin of BiVO4 photoanodes with FeNi oxyhydroxides for oxygen evolution." *Angew. Chemie - Int. Ed.*, **59**, 18990 (2020).
44. X. Yin, Q. Liu, Y. Yang, Y. Liu, K. Wang, Y. Li, D. Li, X. Qiu, W. Li, and J. Li, "An efficient tandem photoelectrochemical cell composed of FeOOH/TiO2 /BiVO4 and Cu2O for self-driven solar water splitting." *Int. J. Hydrogen Energy*, **44**, 594 (2019).
45. Z. Chen, H. N. Dinh, and E. Miller, *Photoelectrochemical Water Splitting: Standards, Experimental Methods, and Protocols* (Springer, New York, NY) (2013).
46. A. A. Jelle, M. Hmadeh, P. G. O'Brien, D. D. Perovic, and G. A. Ozin, "Photocatalytic properties of all four polymorphs of nanostructured iron oxyhydroxides." *ChemNanoMat.*, **2**, 1047 (2016).
47. A. Shoneye and J. Tang, "Highly dispersed FeOOH to enhance photocatalytic activity of TiO2 for complete mineralisation of herbicides." *Appl. Surf. Sci.*, **511**, 145479 (2020).
48. W. Han, L. Ren, L. Gong, X. Qi, Y. Liu, L. Yang, X. Wei, and J. Zhong, "Self-assembled three-dimensional graphene-based aerogel with embedded multifarious functional nanoparticles and its excellent photoelectrochemical activities." *ACS Sustain. Chem. Eng.*, **2**, 41 (2014).
49. J. Xie, P. Yang, X. Liang, and J. Xiong, "Self-improvement of Ti:Fe2O3 photoanodes: photoelectrocatalysis improvement after long-term stability testing in alkaline electrolyte." *ACS Appl. Energy Mater.*, **1**, 2769 (2018).
50. J. Lee, H. Lee, and B. Lim, "Chemical transformation of iron alkoxide nanosheets to FeOOH nanoparticles for highly active and stable oxygen evolution electrocatalysts." *J. Ind. Eng. Chem.*, **58**, 100 (2018).